Geophysical Journal International

Geophys. J. Int. (2021) **227,** 1612–1623
Advance Access publication 2021 August 05
GJI Gravity, Geodesy and Tides

https://doi.org/10.1093/gji/ggab307

Local separation of potential field anomalies using equivalent sources: application for the 3-D structure of mantle uplift beneath Von Kármán crater, the Moon

Yi Zhang [1], Yixian Xu [1], Walter D. Mooney[2] and Chao Chen[3]

[1]*Key Laboratory of Geoscience Big Data and Deep Resource of Zhejiang Province, School of Earth Sciences, Zhejiang University, Hangzhou* 310027*, China. E-mail: zhangyiss@icloud.com*
[2]*Earthquake Science Center, United States Geological Survey, Reston, VA 20192, USA*
[3]*Hubei Subsurface Multi-Scale Imaging Key Laboratory, Institute of Geophysics and Geomatics, China University of Geosciences, Wuhan* 430074*, China*

Accepted 2021 July 29. Received 2021 July 29; in original form 2021 April 27

SUMMARY

The separation of regional-residual anomalies plays an important role in the processing of potential field anomalies for obtaining better understandings of the nature of the underground sources. Many methods have been developed to achieve the separation of anomalies that are of distinct wavelengths. On the other hand, fewer studies have addressed the separation of local anomalies from the observed potential field anomalies. In this paper, we introduce a new process for separating localized anomalies from the observations under the Cartesian and spherical coordinates. The separation is achieved using the equivalent source technique and an iterative inversion process which is to refine and finalize the separated local anomalies. Additionally, we introduce an inversion method for determining the equivalent sources that are of varying dimensions, as well as a quantitative measurement to assess the accuracy of the separation process. Verified with synthetic examples, the proposed method could extract arbitrary shaped local anomalies from the rest with low error levels. Subsequently, we apply the method to the construction of a 3-D model of the mantle uplift beneath the Von Kármán crater (VKC) on the Moon. The VKC is the landing site of the Chinese lunar exploration mission Chang'e 4, which lies in the northwestern portion of the South-Pole Aitken (SPA) basin on the far side of the Moon. Multiple generations of mare basalts are identified within the VKC, which indicates a complex geological history of the basin. Insights into the evolutionary history of this region can be obtained by investigating the deep crustal structure of the VKC using topographic and gravity data. Processed with the proposed method, the 3-D structure we obtain provides evidence for separated mantle uplifting events triggered by the two impact events that created the VKC and the Von Kármán M crater, respectively.

Key words: Magnetic anomalies: modelling and interpretation; Inverse theory; Numerical approximations and analysis; Planetary interiors; Impact phenomena.

1 INTRODUCTION

The observed potential field data are composed of the superposition of gravity or magnetic effects from overlapped subsurface sources, whose individual anomalies might be difficult to extract. For local investigations that utilize potential field data, the targeted objects are usually small-scale density or magnetic structures buried at shallow depths. Anomalies of these shallow sources, which are commonly referred to as residual anomalies, are embedded in anomalies at larger scales and are often deemed to be produced by deeper buried potential field sources. Such anomalies that represent the large-scale character of the observed potential field are usually categorized as regional anomalies. The estimation and separation of targeted anomalies from the total observations expose more clearly the geometry and amplitudes of the anomalies. This in turn leads to better interpretations of the anomalies. Therefore, the separation of regional-residual anomalies is a valuable step in the interpretation of potential field data and has undergone rapid development in the last decades.

In general, techniques that aim to separate regional and residual anomalies fall into two categories. The first approaches are mostly data-based methods that utilize differences of graphic features or signal frequencies between the regional and residual anomalies to achieve their separation. Beltrão *et al.* (1991) introduced the estimation of regional gravity anomalies using the polynomial fitting, while Mickus *et al.* (1991) suggested using the minimum-curvature

technique to separate the regional and residual gravity anomalies. A finite-element method was introduced by Mallick & Sharma (1999) for calculating the regional anomalies. Meanwhile, Zhang *et al.* (2009) proposed the use of 3-D principal components and textural analysis for the separation of potential field data. Besides, the bidimensional empirical mode decomposition method was applied to the problem by Hou *et al.* (2012). For frequency-domain methods, Pawlowski & Hansen (1990) applied the Wiener filter for separating gravity anomalies, which is applied to study density variations within the south polar layered deposits on Mars by Li *et al.* (2012a), and a nonlinear filter method was introduced by Keating & Pinet (2011). Forootan & Kusche (2012), applied the independent component analysis to separate satellite gravity anomalies. In addition to frequency techniques, the wavelet analysis has also been used to perform the separation of potential field data by Fedi & Quarta (1998), Ucan *et al.* (2000) and Xu *et al.* (2009).

The other category includes model-based methods that utilize inherent features of the potential field to separate the regional and residual anomalies. Jacobsen (1987) proposed using the upward continuation of the potential field as a standard separation filter, which is improved by Zeng *et al.* (2007) for the determination of the optimum height for the continuation. Moreover, Pilkington & Cowan (2006) introduced a model-based process to construct optimized filter parameters for separating magnetic data. Albora *et al.* (2001) proposed a cellular neural network approach for the separation of magnetic fields. Meanwhile, the equivalent source technique of the potential field has also been applied to the problem. Chapin (1996) employed the technique to correct isostatic effects in gravity data over the South American Continent. Pawlowski (1994) proposed a method for constructing bandpass filters for gravity data using the equivalent-layer concept, which is also adopted by Guo *et al.* (2013) to build a preferential filter to separate the regional and residual anomalies.

Despite the abundant choices of available methods, the separated anomalies are not easy to evaluate in real-world applications due to the lack of a quantifiable measurement. As the choice of the optimally separated anomalies remains somewhat subjective, the application of multiple methods is recommended for practical uses to ensure optimized results (Keating *et al.* 2011; Martín *et al.* 2011; Martínez-Moreno *et al.* 2015). On the other hand, as pointed out by Li & Oldenburg (1998), most methods for the separation of potential field anomalies focused on anomalies that are produced by sources with distinct burial depths. Fewer efforts have been made to address the separation of local anomalies from the observed anomalies that are composed of similar wavelengths. Such separations are of significance for further extracting the geometric and physical properties of the targeted anomalies. However, as the anomalies are of similar wavelengths, methods that are based on frequency differences cannot yield promising results. To address the problem, Li & Oldenburg (1998) suggested using 3-D inversion results for separating local magnetic data, which is applied to investigate volcanic units in a basin environment (Li *et al.* 2012b). However, in addition to the enormous computational requirements, the 3-D inversion of potential field data is still problematic and cannot produce reliable underground density or magnetic structures easily. Consequently, such an approach is hard to apply in practical investigations. A localized separation of magnetic data is introduced by Fedi & Quarta (1998) using wavelet analysis. Both synthetic and field examples indicate the method could separate the local anomalies from the observations if an appropriate wavelet base is applied to the data. Moreover, for potential field data over large geographic ranges, Wieczorek & Simons (2005) developed a localized spherical harmonic analysis method using a multitaper spectral analysis approach. Localized signals within a selected window could be extracted by filtering out the outside signals in the spherical harmonic domain. Still, such methods do not provide an estimation of the errors of the separation, and therefore, are unable to access the quality of the separated anomalies. Additionally, since the wavelet and spherical harmonic analyses are inherently signal processing techniques, the physical plausibility of the generated anomalies is not always guaranteed.

To contribute to the solution, we propose an innovative approach for separating potential field anomalies of similar wavelengths. The proposed method is built on the equivalent source technique and uses an iteration process to optimize the separated anomalies. Moreover, quantitative measurement is introduced for evaluating the separated anomalies, as well as reducing the subjectivity of the choice of separated anomalies. Evaluated with synthetic data, the proposed method is applied to construct a 3-D mantle uplift model of the Von Kármán crater (VKC) region of the Moon. The VKC is a Nectarian impact crater (Losiak *et al.* 2009; Yingst *et al.* 2017) that lies in the northwestern South Pole-Aitken (SPA) basin (Pasckert *et al.* 2018) on the far side of the Moon. The Chinese lunar exploration mission Chang'e 4 (CE-4; Wu *et al.* 2017) landed on the southern floor of the VKC on 2019 January 3 to carry out *in situ* measurements of spectral, radar and low-frequency radio spectral data in the landing region. Our investigation of the deep crustal structure of the VKC is motivated by the goal of gaining a better understanding of the evolutionary history of the region and better interpretations of the CE-4′s data. Due to a higher density of the lunar mantle compared to the overlying crustal materials, positive gravity anomalies are usually observed at giant impact craters on the Moon (Zuber *et al.* 1994; Neumann *et al.* 1996; Melosh *et al.* 2013), which are associated with mantle uplifts caused by the impact events. Consequently, such anomalies provide valuable opportunities for us to study the spatial structures of the mantle uplifts. However, gravity anomalies produced by the uplifted mantle are commonly overlapped with gravity signals of other sources, such as the undulant topography and the Moho of the Moon as well as subsurface density heterogeneities. In the application, we employ gravity and topographic data of the VKC area to separate local gravity anomalies that are associated with the uplifted mantle within the region. Subsequently, the structure of the 3-D mantle uplift is obtained using an interface inversion method (Zhang *et al.* 2019). An interpretation of the obtained uplift model is given, as well as possible directions for further research.

2 METHODOLOGY

As demonstrated by Dampney (1969), the observed potential field anomalies could be synthesized by a set of equivalent sources, which are normally presented as a layer (or layers) of discrete model elements (Li *et al.* 2019). The physical properties of the element could be determined by using some inversion methods so that the observations could be reproduced by those synthetic sources. Such a technique is of great importance as it could be employed to process the anomalies for various purposes with low error levels, including the upward and downward continuation of the anomalies (Li 2001; Barnes & Lumley 2011), the projection of potential field data onto a horizontal reference plane (Xia & Sprowl 1991; Cooper 2000), estimation of the burial depth of underground sources (Mauriello & Patella 2001; Mikhailov *et al.* 2007) and enhancement of the

measured geoid (Guspí *et al.* 2004). Moreover, since the equivalent technique is based on only the inherent characteristics of the potential field, it could be applied in both the Cartesian and spherical coordinates using different model elements (von Frese *et al.* 1981; Li *et al.* 2019). In this section, we introduce the methodology of our method, including the basic separation scheme, the refinement process and the inversion formulae. Construction of the initial equivalent sources is also discussed subsequently.

2.1 Initial separation

We now consider some anomalies data $\mathbf{d}$ and their equivalent sources $\mathbf{m}$. As shown in Fig. 1, the anomalies $\mathbf{d}$ are produced by two polyhedral sources and show two anomalies with individual peaks at similar wavelengths. To separate the anomalies $\mathbf{d}^{\text{loc}}$ from $\mathbf{d}$, we divide $\mathbf{m}$ into two groups, one includes equivalent sources, that is the local sources $\mathbf{m}^{\text{loc}}$, that are approximately placed under the anomalies $\mathbf{d}^{\text{loc}}$. Meanwhile, the rest sources are gathered as the other group that is referred to as the remaining sources $\mathbf{m}^{\text{rem}}$. The anomalies produced by $\mathbf{m}^{\text{rem}}$ are referred to as the remaining anomalies $\mathbf{d}^{\text{rem}}$. In this case, the separation could be expressed simply as:

$$\mathbf{d} = \mathbf{d}^{\text{loc}} + \mathbf{d}^{\text{rem}} = f\left(\mathbf{m}^{\text{loc}}\right) + f\left(\mathbf{m}^{\text{rem}}\right), \tag{1}$$

in which, f represents a forward modelling operator and $\mathbf{m} = \mathbf{m}^{\text{loc}} \cup \mathbf{m}^{\text{rem}}$. This process could be achieved by inverting the anomalies data into its equivalent sources first, then forward modelling anomalies of the local and remaining sources, respectively. An inverse algorithm that is designed to determine the physical properties of the equivalent sources is introduced in detail in the following section.

Such a process is rather simple and intuitive. However, as physical properties of the equivalent sources are different from those of the actual potential field sources, for example the two polyhedral sources in Fig. 1. The chosen $\mathbf{m}^{\text{loc}}$ very often do not contain just enough information to reproduce the correct local anomalies, that is anomalies of the polyhedral source on the right, and at the same time, have minimal distortions from the rest anomalies. Similarly, it is also hard to guarantee that $\mathbf{d}^{\text{rem}}$ only possess anomalies that are produced by the left polyhedral source. Therefore, it is reasonable to deduce that the separated local and remaining anomalies would normally contain certain portions of the other. Therefore, such a direct separation of local-remaining anomalies might have a lack of accuracy and cannot be put into practical applications directly. Consequently, we see that a refinement process is in need to ensure optimized results and quantifiable measurements of the accuracy should be introduced to validate the separated anomalies.

2.2 Iterative refinement process

To improve the separated local anomalies obtained from a direct separation using eq. (1), we implement the following iteration process (Fig. 2). Taking $\mathbf{d}^{\text{loc}}$ and $\mathbf{d}^{\text{rem}}$ as new observations, respectively, the anomalies could be separated into their own local and remaining components using the direct separation scheme, which is expressed as:

$$\mathbf{d}_i^{\text{loc}} = \mathbf{d}_i^{\text{loc\_loc}} + \mathbf{d}_i^{\text{loc\_rem}} = f\left(\mathbf{m}_i^{\text{loc\_loc}}\right) + f\left(\mathbf{m}_i^{\text{loc\_rem}}\right), \tag{2}$$

$$\mathbf{d}_i^{\text{rem}} = \mathbf{d}_i^{\text{rem\_loc}} + \mathbf{d}_i^{\text{rem\_rem}} = f\left(\mathbf{m}_i^{\text{rem\_loc}}\right) + f\left(\mathbf{m}_i^{\text{rem\_rem}}\right), \tag{3}$$

where $i \geq 0$ represents the iteration times. $\mathbf{d}_i^{\text{loc\_loc}}$ is the local component of $\mathbf{d}^{\text{loc}}$ and $\mathbf{d}_i^{\text{loc\_rem}}$ is the remaining component. Similarly, $\mathbf{d}_i^{\text{rem\_loc}}$ and $\mathbf{d}_i^{\text{rem\_rem}}$ represent the local and remaining components of $\mathbf{d}^{\text{rem}}$, respectively. Equivalent sources of the components are expressed as $\mathbf{m}_i^{\text{loc\_loc}}$, $\mathbf{m}_i^{\text{loc\_rem}}$, $\mathbf{m}_i^{\text{rem\_loc}}$ and $\mathbf{m}_i^{\text{rem\_rem}}$, respectively. Since the potential field decays rapidly with distance from its source, both $\mathbf{d}^{\text{loc}}$ and $\mathbf{d}^{\text{rem}}$ are inclined to be reproduced by close equivalent sources while they are being inverted into physical properties of the sources. Therefore, $\mathbf{d}^{\text{loc}}$ and $\mathbf{d}^{\text{rem}}$ would mostly be represented by the sources $\mathbf{m}_i^{\text{loc\_loc}}$ and $\mathbf{m}_i^{\text{rem\_rem}}$. On the other hand, $\mathbf{m}_i^{\text{loc\_rem}}$ is close to the remaining sources, and $\mathbf{m}_i^{\text{rem\_loc}}$ is near the local anomalies. Consequently, for our separation scheme, it is inferred that $\mathbf{d}_i^{\text{loc\_rem}}$ should contain more remaining anomalies compared to $\mathbf{d}_i^{\text{rem\_loc}}$. Similarly, $\mathbf{d}_i^{\text{rem\_loc}}$ should possess more local anomalies than $\mathbf{d}_i^{\text{loc\_rem}}$. Therefore, we can improve the separated local and remaining anomalies by regrouping the local and remaining components as

$$\mathbf{d}_{i+1}^{\text{loc}} = \mathbf{d}_i{}^{\text{loc\_loc}} + \mathbf{d}_i{}^{\text{rem\_loc}}, \tag{4}$$

$$\mathbf{d}_{i+1}^{\text{rem}} = \mathbf{d}_i{}^{\text{rem\_rem}} + \mathbf{d}_i{}^{\text{loc\_rem}}, \tag{5}$$

Taking $\mathbf{d}_{i+1}^{\text{loc}}$ and $\mathbf{d}_{i+1}^{\text{rem}}$ as new observations, we can separate the local anomalies $\mathbf{d}^{\text{loc}}$ from total anomalies $\mathbf{d}$ iteratively. The iteration process is terminated if $\mathbf{d}_i^{\text{loc\_rem}}$ equals to $\mathbf{d}_i^{\text{rem\_loc}}$ as the separated anomalies cannot be improved anymore, which is determined by

$$\left\|\mathbf{W_d}(\mathbf{d}_i^{\text{rem\_loc}} - \mathbf{d}_i^{\text{loc\_rem}})\right\|^2 \leq 1, \tag{6}$$

where $\mathbf{W}_{\text{d}}$ is an $M \times M$ diagonal matrix in which elements are $1/\sqrt{M}\sigma$, in which M is the number of observations and σ is the uncertainty of the observation. Moreover, we define anomalies $\Delta\mathbf{d} = \mathbf{d}^{\text{rem\_loc}} = \mathbf{d}^{\text{loc\_rem}}$ to represent the uncertainty of the separation. Obviously, both $\mathbf{d}^{\text{loc\_rem}}$ and $\mathbf{d}^{\text{rem\_loc}}$ would be close to zero if the local anomalies are completely extracted. Therefore, we see a measurement $\Delta d = RMS(\Delta\mathbf{d})$ could be used to quantify the separation process, and the smaller the Δd is, the more completeness of the separation is. Following the above iteration process, we could obtain local anomalies that are most spatially separated and the results obtained with different equivalent sources and local-remaining source partitions could be evaluated using the Δd values.

2.3 Inversion formulae

Given some potential field anomalies, they could be inverted into some equivalent sources by solving the following inverse problem:

$$\Phi(\mathbf{m}) = \left\|\mathbf{W_d}(\mathbf{Gm} - \mathbf{d}^{\text{obs}})\right\|^2, \tag{7}$$

in which $\mathbf{G}$ is an $M \times N$ sensitivity matrix that forwards the equivalent sources into potential field data. N is the number of the equivalent sources. The calculation of $\mathbf{G}$ could be determined according to the constructions of the equivalent sources (Nagy 1966; Zhang *et al.* 2018). Eq. (7) ensures that the observed anomalies could be fully reproduced by the equivalent source if it is solved with the criteria $\Phi \leq 1$. In which case, observations are approximated by reproduced data with enough accuracies as their differences are equal to or smaller than the data uncertainties. Equivalent sources $\mathbf{m}$ that minimizes $\Phi(\mathbf{m})$ are found by approaching its zero gradients with respect to $\mathbf{m}$. Therefore, we first derive the gradient of $\Phi(\mathbf{m})$ as

$$\nabla_{\mathbf{m}}\Phi(\mathbf{m}) = \nabla_{\mathbf{m}}\left[\left(\mathbf{Gm} - \mathbf{d}^{\text{obs}}\right)^T \mathbf{W_d}^T \mathbf{W_d}\left(\mathbf{Gm} - \mathbf{d}^{\text{obs}}\right)\right] = 0. \tag{8}$$

Subsequently, eq. (8) is reorganized as

$$\mathbf{Am} = \mathbf{B}, \tag{9}$$

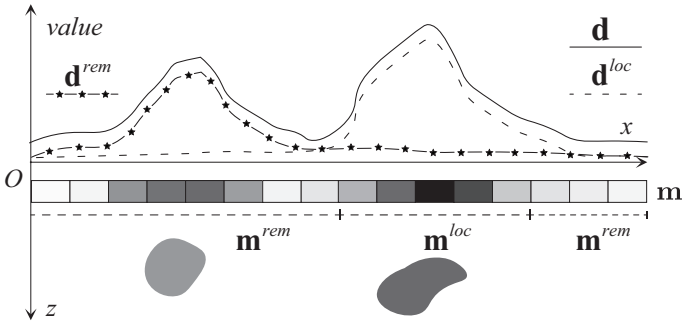

Figure 1. Diagrammatic sketch of using equivalent sources to separate the local anomalies from the observed potential field anomalies **d**. Actual sources of the anomalies are represented as two polygons. Meanwhile, equivalent sources **m** are represented as a layer of rectangular boxes, which are composed of the local sources $\mathbf{m}^{\mathrm{loc}}$ and remaining sources $\mathbf{m}^{\mathrm{rem}}$. In this case, anomalies produced by the sources are referred to as the local anomalies $\mathbf{d}^{\mathrm{loc}}$ and remaining anomalies $\mathbf{d}^{\mathrm{rem}}$, respectively. See the text for further explanations.

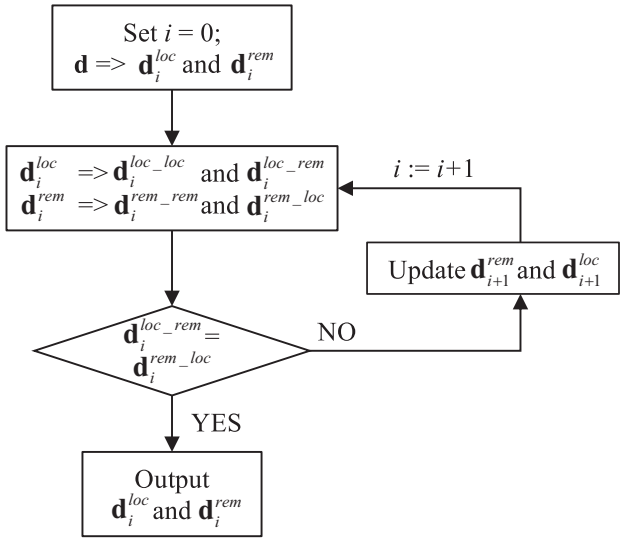

Figure 2. Flow chart of the iteration process for improving the separated local and remaining anomalies. Shown in the figure, symbols => indicate the separation of anomalies. The process is terminated if $\mathbf{d}_i^{\mathrm{loc\_rem}} = \mathbf{d}_i^{\mathrm{rem\_loc}}$. Otherwise, the local and residual anomalies are updated for the next iteration.

in which $\mathbf{A} = \mathbf{G}^T \cdot \mathbf{W_d}^T \mathbf{W_d} \cdot \mathbf{G}$ and $\mathbf{B} = \mathbf{G}^T \cdot \mathbf{W_d}^T \mathbf{W_d} \cdot \mathbf{d}^{\mathrm{obs}}$. Known that the potential field decays fast with the observation distance, and the change of model elements' volume arise different sensitivities of the element's forward modelling data, weights on the elements are added into eq. (9) as a pre-conditioning matrix **P** (Davis & Li 2011; Liu *et al.* 2013). Consequently, the inversion formula is given as

$$\mathbf{PAm} = \mathbf{PB}. \tag{10}$$

The implementation of **P** in eq. (10) is to relieve the attenuation of **A** caused by varying observation distances and different volumes of the model elements, and therefore, stabilize the solving process and minimize acceptable solutions. Subsequently, the precondition matrix **P** is defined as

$$\mathbf{P} = \frac{1}{\mathbf{W_r} \cdot \mathbf{W_v}}, \tag{11}$$

where $\mathbf{W_r}$ and $\mathbf{W_v}$ are two $N \times N$ diagonal matrices of model weights on the observation distances and elements' volume, respectively. Their expressions are given as

$$\mathbf{W}_{\mathbf{r}j} = \left| \sum_{i=1}^{M} \frac{\cos(\theta_{ij})}{(r_{ij} + c_0)^3} \right|^{\alpha/2}, \tag{12}$$

$$\mathbf{W}_{\mathbf{v}j} = \left(v_j / v_{\max}\right)^{\beta}, \tag{13}$$

in which $j = 1, 2, \ldots, N$. r_{ij} is the distance between the ith observation point and the jth model element and θ_{ij} is the angle between $\vec{r}_{ij}$ and the downward z-axis direction. c_0 is a small positive number that validates the equation. A bigger value of the exponential factor α yields heavier weights on distant model elements, which is usually given between 0.5 and 1.5 for gravity data (Li & Oldenburg 2000). Moreover, v_j is the volume of the jth model element and $v_{\max}$ represents the maximal volume among all model elements. The exponential factor β controls volumetric weights on the model elements. Considering a model element with some distance to an observation point, the potential field has nearly a linear relationship with the element's volume. Therefore, the value of β is commonly given as 1.0. Subsequently, a pre-conditioned conjugate gradient method is employed to solve the inverse problem (Kaasschieter 1988).

2.4 Construction of the equivalent sources

As it is demonstrated above, the separated local and remaining anomalies are co-determined by both the geometries of the equivalent source, including their dimensions and burial depth, and the partition of local and remaining sources. Consequently, an optimal combination of the two factors would lead to a separation with minimal Δd values. For the geometries of the equivalent sources, model elements with the form of a right rectangular prism are commonly described using Cartesian coordinates (Li & Oldenburg 1998); spherical triangular and rectangular prisms may also be described with spherical coordinates (Liang *et al.* 2014; Zhang *et al.* 2019). To fully represent the observed anomalies, enough lateral resolution of the sources must be given. More specifically, model elements of the equivalent layer should be small enough to reproduce the observed anomalies of the shortest wavelength. Practically, the resolution of the equivalent sources is adequate if it is not less than the spatial resolution of the processing anomalies data. On the other hand, we seek to optimize the separation that is quantified by Δd. Therefore, the depth of the equivalent layer should be chosen in a way that minimizes Δd. As demonstrated by Mauriello & Patella (2001), for an individual potential field source, its equivalent sources have the most compacted physical properties when the equivalent layer is approximately placed at the same depth as the

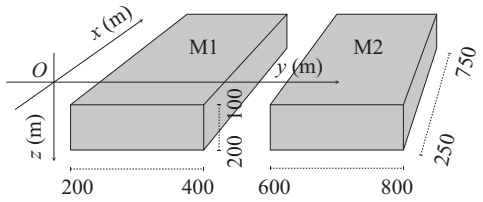

Figure 3. Diagrammatic sketch of block model M1 and M2's dimensions. The block models are placed in the right-handed Cartesian coordinate system with the *x*-axis pointing north and the *z*-axis pointing vertically downwards. The strength of the geomagnetic field is given as 5e + 4 nT.

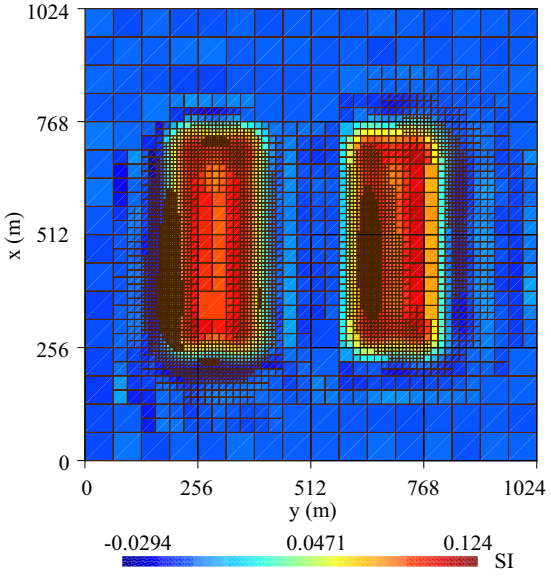

Figure 4. Equivalent sources of the synthetic magnetic data. Spatial constructions of the equivalent layer used in the example are represented as black rectangles.

actual sources. Subsequently, it will be easier to separate the local anomalies. Therefore, the preferable depth of the equivalent sources for the separation is most likely to be found around the estimated source depth of the potential field anomalies being modelled (Maus & Dimri 1996). Meanwhile, for the partition of the local and remaining sources, a good way to set up the area of the local sources is to cover the targeted anomalies as completely as possible, such as along the zero contours or through the saddle area of adjacent anomalies. Once the initial parameters of the equivalent source layer are determined, they are adjusted in a way that minimizes Δd, which is normally completed through trial and error.

3 SYNTHETIC EXAMPLES

3.1 Separation of the magnetic anomalies

We first evaluate the proposed method with synthetic magnetic and gravity anomalies. Two block models M1 and M2 (Fig. 3) are employed in the first example to forward synthetic magnetic ΔT anomalies which represent the total magnetic force anomalies.

For the construction of the equivalent sources, model elements in the form of a right rectangular prism are employed (Fig. 4). Different prism sizes are utilized to improve the computational efficiencies according to absolute values of the observed anomalies' lateral gradients. Small model elements are employed where the anomalies show higher gradients. Meanwhile, larger model elements are placed where the anomalies have lower changing rates. Therefore, we ensure that the observed anomalies could be approximated with high accuracy while keeping the inverse problem at relatively small scales. In a practical matter, such structures could be obtained using a quad-tree algorithm (Davis & Li 2011). We also show equivalent sources of the synthetic ΔT anomalies derived from the direct separation scheme to demonstrate the effectiveness of the proposed inversion algorithm. Central depth and thickness of the equivalent layer used in the inversion are expressed in bold faces in Table 1

Table 1. Values of Δd (nT) of different combinations of the equivalent layer's centre depth and thickness utilized in the first synthetic example.

Centre depth (m)	Layer thickness (m)		
	50	100	150
165	3.108	3.521	3.728
175	**2.929**	3.059	3.775
185	3.200	3.074	3.283

We take anomalies produced by M1 as the local anomalies (Fig. 5c), and anomalies of M2 are seen as the remaining positive anomalies shown on the left. Selected from multiple combinations of the equivalent layer's parameters (Table 1), the observed anomalies are separated into the local and remaining anomalies (Figs 5e and f) with a minimal $\Delta d = 2.93$ nT (Fig. 5b).

We observe that the separated local anomalies could fairly restore the synthetic data, differences mainly exist at the negative parts of the local anomalies ones (Fig. 5d). We set the magnetization inclination and declination angles of M1 as 70° and 10°, as the same as the geomagnetic inclination and declination angles. The angles of M2 equal to −30° for inclination and 60° for declination, respectively. In the example, both inclination and declination angles are provided as prior information. As shown in Fig. 5(a), we see positive parts of the synthetic ΔT anomalies are almost mixed by superposition, and consequently, we cannot distinguish the two anomalies from the observations. To separate the two anomalies, the area of the local sources is drawn to cover the (Figs 5c and e). Meanwhile, positive parts of the remaining anomalies are largely recovered with some minor distortions around the original positions of local anomalies (Figs 5d and f). More clearly, we see differences between the separated anomalies, and synthetic data mostly appear at boundaries of the local sources and *RMS* of the differences are about 7 nT for both anomalies (Figs 5g and h). Additionally, we see that the $\Delta\mathbf{d}$ anomalies mainly exist around the boundaries of the local and residual sources as well (Fig. 5b).

3.2 Separation of the gravity anomalies

Additionally, we present a more complex example using synthetic gravity anomalies. The geometries and physical properties of the models are shown in Fig. 6. As we introduced in the last example, different sizes of the model elements are utilized to construct the equivalent layer according to the lateral gradients of the observed gravity anomalies. Spatial constructions of the equivalent layer and equivalent sources of the gravity data derived from the direct scheme are as shown in Fig. 7. The central depth and thickness of the equivalent layer used in the inversion are expressed in bold faces in Table 2.

In this example, we take between the separated and synthetic anomalies are about 2e-2 mGal and the *RMS* of the differences are close to 3.1e-2 mGal, which are relatively small compared to the

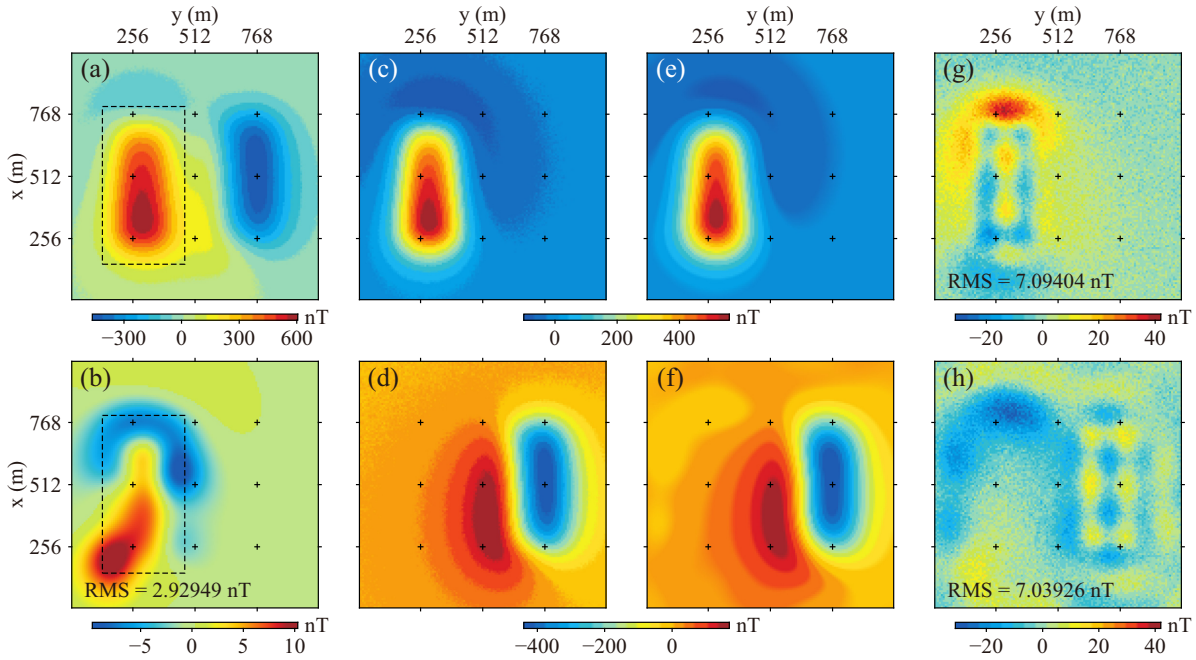

Figure 5. Synthetic and separated ΔT anomalies of the first synthetic example. The anomalies are calculated at zero altitudes. The central depth and thickness of the equivalent layer used in the separation are equal 175 and 50 m, respectively. (a) Synthetic magnetic anomalies with Gaussian noises that are of zero means and 2 nT standard deviations. The area of the local sources is shown as a dotted black rectangle. (b) $\Delta\mathbf{d}$ anomalies of the separation. (c and d) Synthetic local and remaining anomalies. (e and f) Separated local and remaining anomalies. (g and h) Differences between the separated and synthetic local and remaining anomalies, respectively.

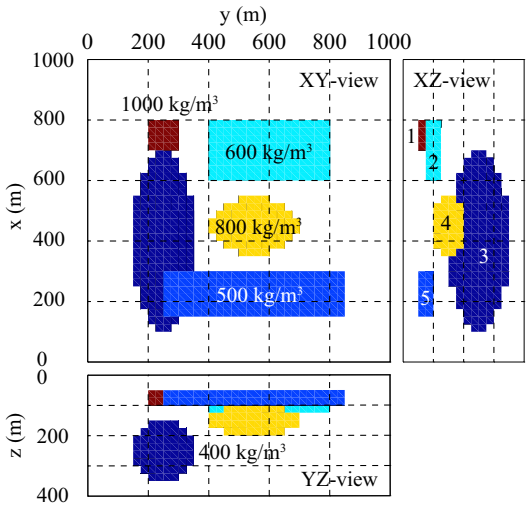

Figure 6. Side views of five block models used in the second synthetic example. Three different perspectives are shown in the figure, including the XY, XZ and YZ views. The blocks are marked as #1 to #5 and their physical properties are as shown in the figure.

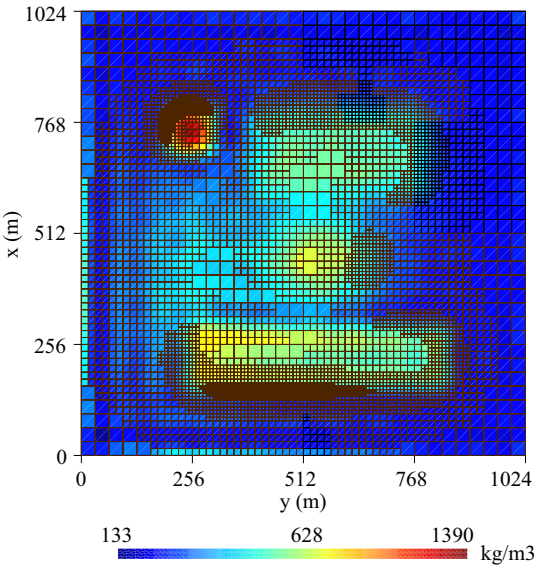

Figure 7. Equivalent sources of the synthetic gravity data. Spatial constructions of the equivalent layer used in the example are represented as black rectangles.

observations (Figs 8g and h). And a minimal Δd = 5.94e-3 mGal is found for the separation (Fig. 8b). Statistics of the separation are given in Table 2.

Demonstrated by the examples, we see the proposed anomalies produced by models #1 and #4 as the local anomalies (Fig. 8c). And anomalies of the other three models are seen as the remaining anomalies (Fig. 8d). As shown in Fig. 8(a), the total gravity anomalies are composed of several anomalies of different scales that are overlapped with each other. The area of the local sources is drawn through the saddle areas of adjacent anomalies (Fig. 7).

Table 2. Values of Δd (mGal) of different combinations of the equivalent layer's centre depth and thickness utilized in the second synthetic example.

Centre depth (m)	Layer thickness (m)		
	30	**40**	50
65	6.69e-3	6.66e-3	6.62e-3
75	7.98e-3	**5.94e-3**	5.99e-3
85	6.53e-3	8.18e-3	6.99e-3

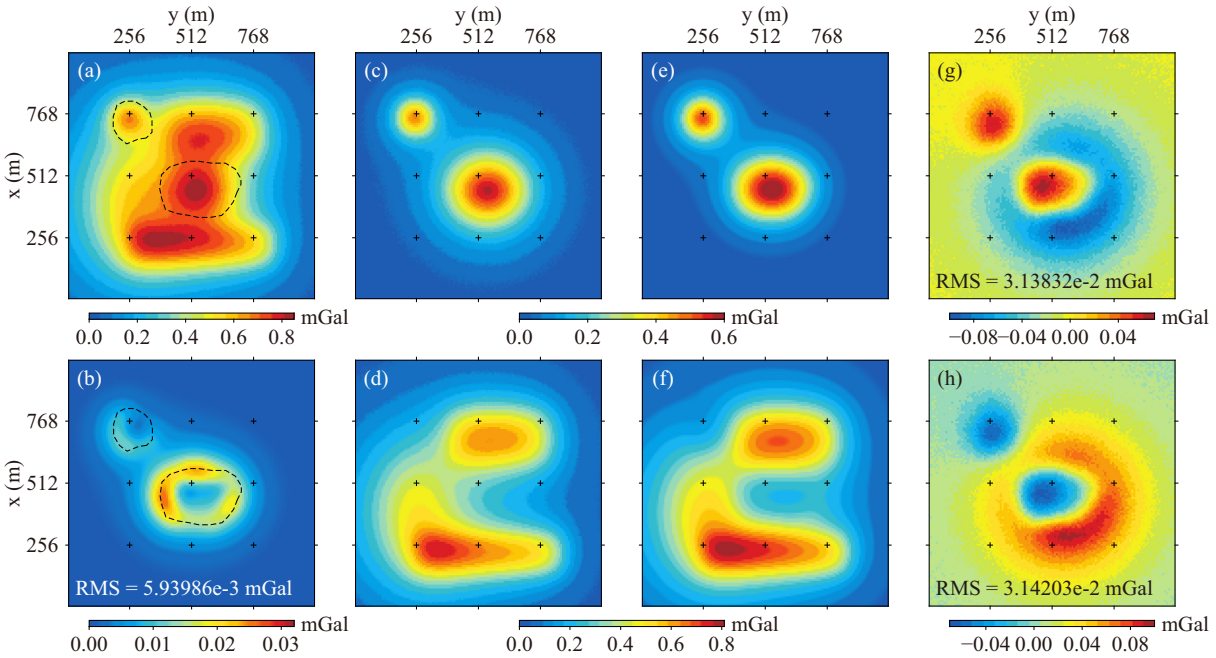

Figure 8. Synthetic and separated gravity anomalies of the second synthetic example. The anomalies are calculated at zero altitudes. The central depth and thickness of the equivalent layer used in the separation are equal 75 and 40 m, respectively. (a) Synthetic gravity anomalies with Gaussian noises that are of zero mean and 2e-3 mGal standard deviation. Areas of the local sources that are used for the separation are surrounded by dashed lines. (b) $\Delta\mathbf{d}$ anomalies of the separation. (c and d) Synthetic local and remaining anomalies. (e and f) Separated local and remaining anomalies. (g and h) Differences between the separated and synthetic local and remaining anomalies, respectively.

As seen in the figures, the separated local and residual anomalies could mostly restore the synthetic (Figs 8e and f), respectively. Differences between the separated and synthetic anomalies are mostly shown around the boundaries of the local and remaining sources (Fig. 8b). Statistically, the mean differences method could separate potential field anomalies of similar wavelengths with good accuracy. Errors of the separation mostly exist at the boundaries of the local and residual sources. Differences between the separated and synthetic are relatively small compared to the observations. The implementation of Δd values provides quantitative measurements for evaluating the separation. And subjective preferences are minimized as the preferable separated anomalies are chosen according to an objective criterion.

4 3-D STRUCTURE OF THE MANTLE UPLIFT BENEATH THE VKC

In this section, we employ the proposed method to separate local gravity anomalies in the VKC region that are deemed to be associated with the mantle uplift. The 3-D structure of the mantle uplift is then obtained using an inversion method for density interface using the spherical coordinates. Interpretations of the resultant 3-D structures are given subsequently.

4.1 Topographic and geological characteristics

The VKC (176.3°E/44.45°S; diameter: ∼186 km) is a degraded Nectarian (∼3.9 Ga) impact crater (Huang *et al.* 2018) located on the far side of the Moon. It is in the northwestern part of the SPA basin, which is the largest known impact structure in the solar system (Fig. 9). In general, higher elevations are found in the northwestern part of the study area, while the southeastern area has lower altitudes

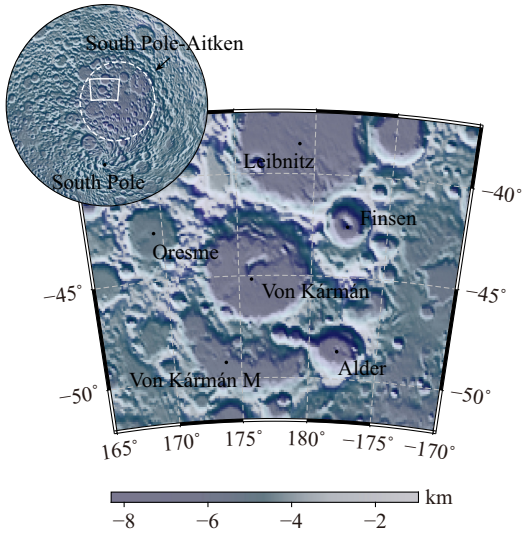

Figure 9. The topography of the study area is represented by a calculation up to 1440 degrees/orders of spherical harmonics of the GSFC lunar topography model LRO_LTM05 (Smith *et al.* 2010). Locations of the VKC and other major caters in the area are labelled. The upper-left-hand portion of the figure shows the relative location of the study area (box) to the SPA basin (dashed line).

within the basin. Specifically, the northern third of the VKC is overlain by the southern rim and outer rampart of the Leibnitz crater. Large portions of the VKC's northeastern crater rim and crater floor are covered by the ejecta of the Finsen crater, which would cause a lower FeO content in this area comparing to the other parts of the crater (Pasckert *et al.* 2018). The northwestern rim of the VKC is adjacent to the Oresme crater that was formed pre-Nectarian.

On its southern border, the VKC is superimposed on Von Kármán M crater (VKMC; 176.2°E/47.2°S; diameter: ∼225 km) which is highly degraded and only the southern half of the crater is still visible today. The southeastern rim of the VKC is overprinted by two small craters and the Alder crater. Inside the VKC, aside from the northern part, the crater has a relatively flat floor that is covered by 3.35 Ga mare basalts (Haruyama *et al.* 2009). Pasckert *et al.* (2018) observed older mare units (∼3.75 Ga) in the area that might be related to older buried flows, and mare units are also identified inside the VKMC. The existence of mare units inside the VKC and VKMC suggests mantle uplifting events caused by the impacts that formed the craters billions of years ago. Hence, recovering the 3-D structure of the uplifts would improve our knowledge of the evolutionary history of the region.

4.2 Data processing and separation of local gravity anomalies

We first extract the gravity data for the study area using the lunar gravity model JGGRX_1500E (Lemoine *et al.* 2013) which is made public by the Goddard Space Flight Center, NASA. As is evident in Fig. 10(a), we see that gravity observations within this area are highly correlated with the topography. Maximal values of the gravitational anomalies, about 280 mGal, are found around the northern rim of the VKC which has a relatively high altitude. Elsewhere, within the VKC and other craters, gravity data only show mild variations. Unlike some other giant impact craters with diameters from 200 to 250 km, no obvious positive gravity anomalies that centred on the VKMC or the Leibnitz crater could be observed from the observations (Zuber *et al.* 1994; Baker *et al.* 2017). To estimate the gravity effects of the topography, a multiresolution topography model of the Moon is employed to forward modelling topographic effects on the gravity field in the study area (Fig. 10b). The topography of the area is taken from the GSFC lunar topography model LRO_LTM05 (Smith *et al.* 2010), and an average crustal density of 2856 kg m^{-3} is used for the forward calculation (Wieczorek *et al.* 2013; Zhang *et al.* 2019). The topographic model consists of the highest 0.1° resolution over the study area. Estimated errors of the forward calculated topographic gravity field are less than 0.3 mGal (Zhang *et al.* 2018). Additional gravity effects produced by overlying mare basalts within the VKC and VKMC are neglected here since detailed mare depths of the craters are currently not available. We next obtain the Bouguer gravity anomalies of the area by subtracting topographic gravity effects from the observed gravity data (Fig. 10c). As shown in the figure, we observe obvious positive anomalies at the southern floor and southern rim of the VKC. Besides, some parts of this anomaly extend into the VKMC. It is known that such gravity anomalies caused by impact events are usually located at the centres of the impact craters (Melosh *et al.* 2013). As we demonstrate below, the observed gravity anomaly is most likely to be produced by uplifted mantle materials beneath the VKMC. Moreover, we observe long-wavelength variations of the Bouguer gravity anomalies within the study area. Minimal trends are found northwestern of the area, while higher anomalies are located at the southern and southeastern parts of the study area. Such regional gravity anomalies are usually related to undulating density interfaces such as the Moho or deep density heterogeneities such as the anomalously dense mantle under the southern floor of the SPA basin that is discovered by James *et al.* (2019). Therefore, we subtract regional trends from the Bouguer anomalies using second-order polynomial fitting to obtain residual anomalies (Beltrão *et al.* 1991).

As shown in Fig. 11, we observe obvious positive gravity anomalies centred on the VKMC and Leibnitz crater. Baker *et al.* (2017) classified both the VKMC and the Leibnitz crater as candidate peak-ring basins. Such basins are generally expected to have strong, circular, positive Bouguer anomalies in the centres of the basins along with surrounding annuli of negative anomalies. However, such negative anomalies are very hard to see at the VKMC. This might be caused by the resurfacing of the mare over inside peak-rings of the basins and the surrounding annuli of negative anomalies are cancelled out by positive anomalies caused by the dense mare basalts. Bouguer anomalies reach a maximum of 162 mGal near the southern rim of the VKC. The anomaly centred on the VKMC is nearly pear-shaped with some extensions to the north towards the centre of the VKC. Yet, we cannot observe obvious gravity anomalies centred within the VKC, and therefore, it is unclear whether there exists obvious mantle uplift beneath the VKC (Soderblom *et al.* 2015). However, we see substantial negative gravity anomalies around the eastern rim crest of the VKC and Alder crater, where are too far away to be related to the subsurface structure of the VMC and VKMC. Also, no obvious negative anomalies are evident elsewhere in the region surrounding the positive anomaly. Moreover, unlike most parts of the SPA basin that are enriched with pyroxene, the Alder crater is dominated by anorthosite rock that has a lower density than pyroxene (Pieters *et al.* 2001). Therefore, we deem that the observed negative gravity anomalies are likely to be related to lower crust densities around the Alder crater and the high porosity areas near the eastern rim of the VKC. Subsequently, to eliminate the effects of these negative anomalies in the following interface inversion, we employ the proposed method to extract the positive anomalies.

Equivalent sources of the separation are constructed using model elements in the form of spherical triangular prisms for the structural representation. Multiple sizes of the model elements are utilized to improve the computational efficiencies (Zhang *et al.* 2018). The area of the local sources is slightly larger than the observed local anomaly, which is delineated using total horizontal gradients of the residual Bouguer anomalies of the study area (Fig. 10). Equivalent sources of the residual Bouguer anomalies are shown in Fig. 12. The top and bottom depths of the equivalent layer used in the inversion are expressed in bold faces in Table 3.

Following the process that we introduced in the previous sections, we separate local gravity anomalies (Fig. 13a) caused by the uplifted mantle beneath the VKC and VKMC from the residual Bouguer anomalies (Fig. 11). The top and bottom depths of the equivalent source layer used for the separation are 0.6 and 37 km, respectively. Different combinations of the equivalent source's setup are implemented to find the optimized parameters, which are shown in Table 3. Maximal values of the local gravity anomalies are about 165 mGal which is slightly larger than those shown in Fig. 11 because the separation process recovers offsets between the original positive gravity anomaly and the nearby negative gravity anomalies. The local gravity anomalies show similar features to those seen in the residual Bouguer anomalies (Fig. 11). Moreover, as shown in Fig. 13(c), maximal and minimal values of undetermined anomalies Δd are about ± 1.0 mGal, respectively. The corresponding Δd equals 6.23e-2 mGal which yields an RMS value of $\Delta \mathbf{d}$ about 0.06 mGal. Compared to the local anomalies, those undetermined anomalies are minimal, and therefore, are neglected in the following process.

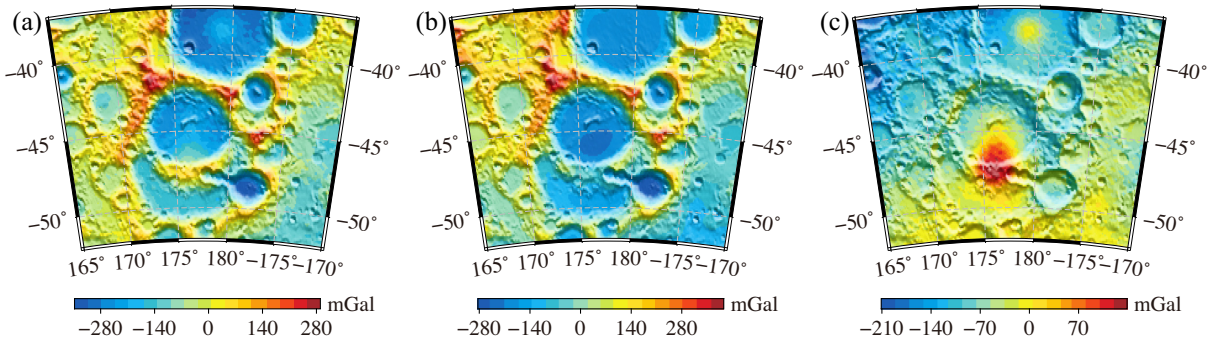

Figure 10. (a) Gravity disturbance of the study area. The gravity data are calculated up to 720 degrees/orders of spherical harmonics at the Moon's reference radius of 1738 km. (b) The topographic gravity effects of the study area are calculated for the reference sphere of the Moon. (c) Bouguer gravity anomalies of the VKC area calculated using gravity data in (a) and (b).

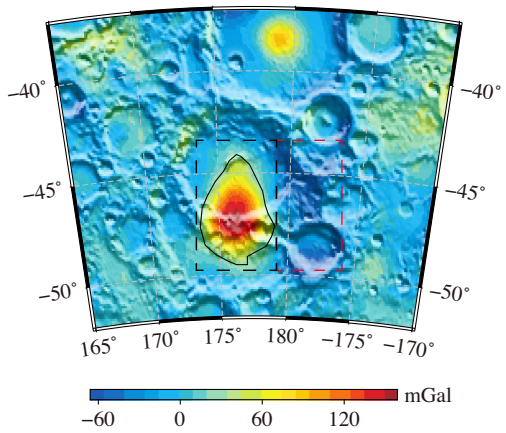

Figure 11. Residual Bouguer gravity anomalies of the study area obtained by removing long-wavelength gravity anomalies (Beltrão *et al.* 1991) from the Bouguer gravity anomalies (Fig. 10c). The area of the local sources is marked by the black polygon. Positive anomalies centred on the VKMC are rounded by the dotted black rectangle. Negative anomalies locate on the eastern rim of the VKC and Alder crater are rounded by the dotted red rectangle.

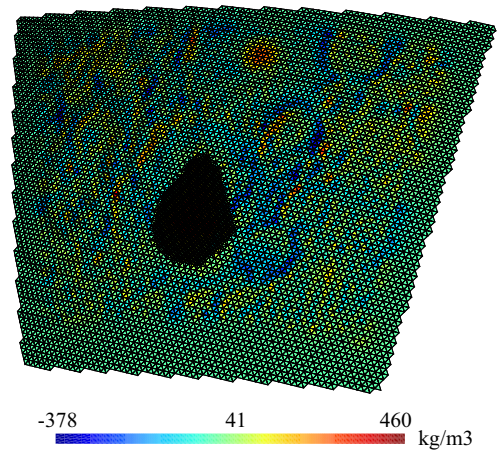

Figure 12. Equivalent sources of the residual Bouguer anomalies. Spatial structures of the equivalent source layer are represented in the form of spherical triangular prisms.

Table 3. Values of Δd (mGal) of different combinations of the equivalent layer's top and bottom depths.

Top depth (km)	Bottom depth (km)		
	32	**37**	42
0.5		6.49e-2	
0.6	6.27e-2	**6.23e-2**	6.26e-2
0.7	6.54e-2	6.49e-2	6.98e-2

4.3 Inversion of the mantle uplift and geophysical interpretation

To obtain a clearer image of the structure of the mantle uplift caused by the impact events of the VKC and VKMC, we invert the local gravity anomalies (Fig. 13a) to obtain the elevations of the mantle uplift using the method introduced by Zhang *et al.* (2019). The inversion is implemented by assuming an average Moho depth of 43 km and an average mantle density of 3356 kg m^{-3} (Zhang *et al.* 2019). Uncertainties of the separated local anomalies are estimated to be around 1.3 mGal and uncertainties of the inverted mantle uplifts are estimated to be about 16 m using a spherical shell with averaged Moho depth and mantle density. We remove long-wavelength gravity variations from the Bouguer gravity anomalies (Figs 10c and 11) and regional anomalies of the residual Bouguer anomalies are separated. The residual local anomalies only reflect the gravitational effects of the uplifted mantle that are the result of the impact events. The inversion result should be taken as estimated mantle uplifts that correspond to a simplified situation, in which case the regional trend of the Moho undulation is neglected and other gravitational anomalies like the positive anomalies at the Leibnitz crater are also overlooked.

The 3-D views of the inverted mantle uplift are shown in Fig. 14. We see an obvious mantle uplift under the southern rim of the VKC which is originally the centre of the VKMC. Therefore, principal mantle uplifts should be caused by the impact event of the VKMC. Possible crustal bulges that are associated with the impact event are observed around the uplifted area with maximal depths to about 50 km. Such structures also consist of the typical crustal structure of a peak-ring basin (Baker *et al.* 2016, 2017; Sood *et al.* 2017). The average elevation of the main uplift is about 20 km deep with maximal values approaching 10 km deep at the edges of the uplift (Fig. 15a). Lower mantle elevations, corresponding to a subsurface depth of about 25 km, are found at the centre of the uplift. Moreover, a significant feature of the uplifts is that, besides the principal uplift, we observe a branch of the uplifted mantle that is located near the centre of the VKC. This structure should correspond to a secondary

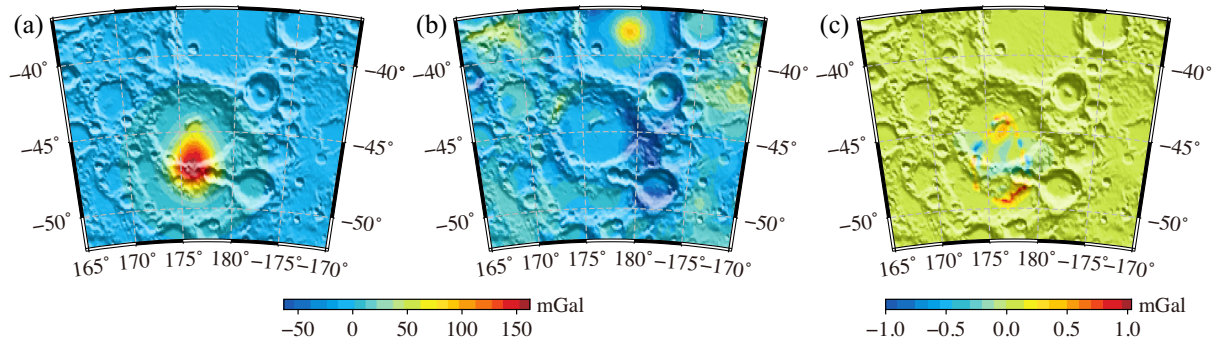

Figure 13. Separated (a) local and (b) regional gravity anomalies of the residual Bouguer anomalies of the area of the VKC. (c) Δ**d** anomalies of the separation.

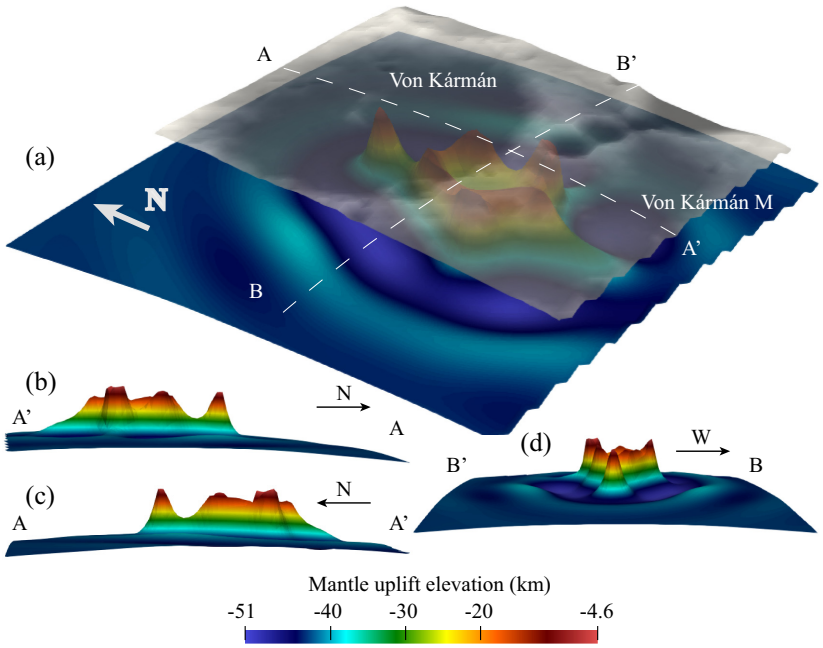

Figure 14. (a) 3-D views of the uplifted mantle obtained from the inversion of gravity data. The locations of profiles AA′ and BB′ are indicated by dashed lines. (b) Side view from S to N. (c) Side view from N to S. (d) Side view from W to E. Surface undulation shown in the figures are not to scale.

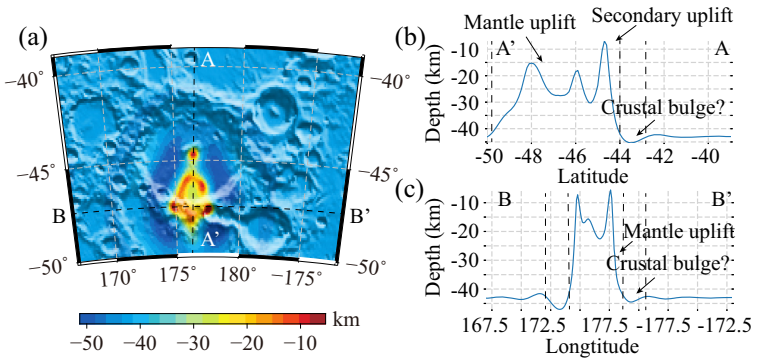

Figure 15. (a) Inverted mantle uplifts with respect to the reference radius of the Moon. Two profiles (b) AA′ and (c) BB′ are shown on the right. The longitude and latitude of AA′ and BB′ are 176.4°E and 47.5°S, respectively. See text for further explanation.

uplifting of mantle materials caused by the impact event of the VKC that happened after the formation of the VKMC. However, we could observe that the secondary uplift is much less significant than the main uplift even though the two basins have similar diameters. A possible reason for such differences is the distinct pre-existing conditions for the impact events. Strengthened crustal structures after the impact event of the VKMC and a different thermal profile could cause more resistance on the impact process of the VKC and lead to reduced mantle uplifts.

To further investigate the geometric features of the uplift structures, we extract two profiles AA′ and BB′ of the inverted mantle structure (Figs 15b and c). The main mantle uplift has a relatively

complex structure. Higher elevations are found at the edges of the principal mantle uplift while lower elevations are located at the centre of the uplift structure. A secondary uplift that is related to the impact event of the VKC is evident at the northern side of the main uplift. Maximal elevation of the secondary uplift surpasses the main uplift to about 5 km. The formation of such structures might be related to the sequence of impact events of the VKMC and VKC, which involves the destruction of the crustal structure of the impact of the VKMC, short-term impact effects of the VMC and long-term post-impact isostatic adjustments of the basins. Further dynamic simulations are needed to constrain the creation of the inverted mantle structure.

5 CONCLUSIONS

In this paper, we introduce a new method for separating local gravity anomalies using equivalent sources. Compared with commonly used techniques such as wavelet analysis or the localized spherical harmonic analysis, the proposed method has certain advantages. The implementation of an objective standard makes it easier to evaluate the products of separation. Additionally, the separated local and remaining anomalies are always physically plausible since the anomalies are calculated from density variations. At the same time, the proposed method is not completely objective in that one still has to determine the area of interested equivalent sources. However, such a task would not be too difficult to accomplish given that it is relatively easy to recognize horizontal boundaries of gravity anomalies, and preferred results could always be chosen with quantitative standards. However, knowing the non-uniqueness of gravity sources, gravity anomalies that are of similar characteristics could be produced by different underground sources with distinct geometric and physical properties. Additional information regarding the sources' nature should be considered to verify the use of the proposed method.

On the other hand, we investigated the 3-D structure of mantle uplift beneath the VKC and VKMC of the Moon. Being the landing site of the lunar probe CE-4, the deep crustal structure of the VKC reflects the evolutionary history of the region and may be used as an aid in the interpretation of CE-4′s data. The 3-D structure of the mantle uplift shows images of two episodes of mantle uplift that correspond to the impact events that formed the VKMC and VKC, respectively. Relatively complex structures are observed in the inverted mantle uplifts. Possible mechanisms of the formation of such structures involve the destruction and reconfiguration of the pre-existing mantle uplift, as a consequence of the precedent impact event that created the VKMC, which is caused by the subsequent impact event that formed the VKC. Impact simulations would give a more comprehensive understanding of the formation process of mantle uplift that is presented here.

ACKNOWLEDGEMENTS

This study is supported by the China Postdoctoral Science Foundation (No. 2020M681824) and the Natural Science Foundation of China (No. 41974082). Support from the US Geological Survey Earthquake Hazards Program is appreciated.

DATA AVAILABILITY

The data and codes associated with this paper can be obtained by contacting the corresponding author.

REFERENCES

Albora, A.M., Özmen, A. & Ucan, O.N., 2001. Residual separation of magnetic fields using a cellular neural network approach, *Pure appl. Geophys.,* **158**(9–10), 1797–1818.

Baker, D.M., Head, J.W., Collins, G.S. & Potter, R.W., 2016. The formation of peak-ring basins: working hypotheses and path forward in using observations to constrain models of impact-basin formation, *Icarus,* **273,** 146–163.

Baker, D.M., Head, J.W., Phillips, R.J., Neumann, G.A., Bierson, C.J., Smith, D.E. & Zuber, M.T., 2017. Grail gravity observations of the transition from complex crater to peak-ring basin on the moon: implications for crustal structure and impact basin formation, *Icarus,* **292,** 54–73.

Barnes, G. & Lumley, J., 2011. Processing gravity gradient data, *Geophysics,* **76**(2), I33–I47.

Beltrão, J.F., Silva, J.B.C. & Costa, J.C., 1991. Robust polynomial fitting method for regional gravity estimation, *Geophysics,* **56**(1), 80–89.

Chapin, D.A., 1996. A deterministic approach toward isostatic gravity residuals: a case study from South America, *Geophysics,* **61**(4), 1022–1033.

Cooper, G., 2000. Gridding gravity data using an equivalent layer, *Comput. Geosci.,* **26**(2), 227–233.

Dampney, C.N.G., 1969. The equivalent source technique, *Geophysics,* **34**(1), 39–53.

Davis, K. & Li, Y., 2011. Fast solution of geophysical inversion using adaptive mesh, space-filling curves and wavelet compression, *Geophys. J. Int.,* **185**(1), 157–166.

Fedi, M. & Quarta, T., 1998. Wavelet analysis for the regional-residual and local separation of potential field anomalies, *Geophys. Prospect.,* **46**(5), 507–525.

Forootan, E. & Kusche, J., 2012. Separation of global time-variable gravity signals into maximally independent components, *J. Geod.,* **86**(7), 477–497.

Guo, L.H., Meng, X.H., Chen, Z.X., Li, S.L. & Zheng, Y.M., 2013. Preferential filtering for gravity anomaly separation, *Comput. Geosci.,* **51,** 247–254.

Guspí, F., Introcaso, A. & Introcaso, B., 2004. Gravity-enhanced representation of measured geoid undulations using equivalent sources, *Geophys. J. Int.,* **159**(1), 1–8.

Haruyama, J. *et al.*, 2009. Long-lived volcanism on the lunar farside revealed by SELENE terrain camera, *Science,* **323**(5916), 905–908.

Hou, W.S., Yang, Z.J., Zhou, Y.Z., Zhang, L.P. & Wu, W.L., 2012. Extracting magnetic anomalies based on an improved BEMD method: a case study in the Pangxidong Area, South China, *Comput. Geosci.,* **48,** 1–8.

Huang, J., Xiao, Z., Flahaut, J., Martinot, M., Head, J., Xiao, X., Xie, M. & Xiao, L., 2018. Geological characteristics of Von Kármán crater, northwestern South Pole-Aitken basin: Chang'e-4 landing site region, *J. geophys. Res.,* **123**(7), 1684–1700.

Jacobsen, B.H., 1987. A case for upward continuation as a standard separation filter for potential field maps, *Geophysics,* **52**(8), 1138–1148.

James, P.B., Smith, D.E., Byrne, P.K., Kendall, J.D., Melosh, H.J. & Zuber, M.T., 2019. Deep structure of the lunar South Pole-Aitken basin, *Geophys. Res. Lett.,* **46**(10), 5100–5106.

Kaasschieter, E.F., 1988. Preconditioned conjugate gradients for solving singular systems, *J. Comput. Appl. Math.,* **24**(1–2), 265–275.

Keating, P. & Pinet, N., 2011. Use of non-linear filtering for the regional-residual separation of potential field data, *J. Appl. Geophys.,* **73**(4), 315–322.

Keating, P., Pinet, N. & Pilkington, M., 2011. Comparison of some commonly used regional residual separation techniques, in *International Workshop on Gravity, Electrical & Magnetic Methods and Their Applications 2011,* Beijing, China, p. 14, Society of Exploration Geophysicists.

Lemoine, F.G. *et al.*, 2013. High–degree gravity models from GRAIL primary mission data, *J. geophys. Res.,* **118**(8), 1676–1698.

Li, D., Liang, Q., Du, J., Sun, S., Zhang, Y. & Chen, C., 2019. Transforming total-field magnetic anomalies into three components using dual-layer equivalent sources, *Geophys. Res. Lett.,* **46**. https://doi.org/10.1029/2019GL084607.

Li, J., Andrews-Hanna, J.C., Sun, Y., Phillips, R.J., Plaut, J.J. & Zuber, M.T., 2012a. Density variations within the south polar layered deposits of Mars, *J. geophys. Res.,* **117**(E4), 1–13.

Li, Y., 2001. Processing gravity gradiometer data using an equivalent source technique, in *SEG Technical Program Expanded Abstracts 2001,* pages 1466–1469, Society of Exploration Geophysicists.

Li, Y. & Oldenburg, D.W., 1998. Separation of regional and residual magnetic field data, *Geophysics,* **63**(2), 431–439.

Li, Y. & Oldenburg, D.W., 2000. Joint inversion of surface and three-component borehole magnetic data, *Geophysics,* **65**(2), 540–552.

Li, Y., He, Z.X. & Liu, Y.X., 2012b. Application of magnetic amplitude inversion in exploration for volcanic units in a basin environment, *Geophysics,* **77**(5), B219–B225.

Liang, Q., Chen, C. & Li, Y., 2014. 3-D inversion of gravity data in spherical coordinates with application to the GRAIL data, *J. geophys. Res.,* **119**(6), 1359–1373.

Liu, S., Feng, J., Gao, W.L., Qiu, L.Q., Liu, T.Y. & Hu, X.Y., 2013. 2D inversion for borehole magnetic data in the presence of significant remanence and demagnetization, *Chin. J. Geophys.,* **56**(12), 4297–4309.

Losiak, A., Wilhelms, D., Byrne, C., Thaisen, K., Weider, S., Kohout, T., O'Sullivan, K. & Kring, D., 2009. A new lunar impact crater database, in *Lunar and Planetary Science Conference,* Vol. 40, The Woolands, TX.

Mallick, K. & Sharma, K.K., 1999. A finite element method for computation of the regional gravity anomaly, *Geophysics,* **64**(2), 461–469.

Martín, A., Núñez, M., Gili, J. & Anquela, A., 2011. A comparison of robust polynomial fitting, global geopotential model and spectral analysis for regional–residual gravity field separation in the Doñana National Park (Spain), *J. Appl. Geophys.,* **75**(2), 327–337.

Martínez-Moreno, F., Galindo-Zaldvar, J., Pedrera, A., Teixid, T., Pea, J. & Gonzlez-Castillo, L., 2015. Regional and residual anomaly separation in microgravity maps for cave detection: the case study of Gruta de las Maravillas (SW Spain), *J. Appl. Geophys.,* **114,** 1–11.

Mauriello, P. & Patella, D., 2001. Localization of maximum depth gravity anomaly sources by a distribution of equivalent point masses, *Geophysics,* **66**(5), 1431–1437.

Maus, S. & Dimri, V., 1996. Depth estimation from the scaling power spectrum of potential fields?, *Geophys. J. Int.,* **124**(1), 113–120.

Melosh, H.J. *et al.*, 2013. The origin of lunar mascon basins, *Science,* **340**(6140), 1552–1555.

Mickus, K.L., Aiken, C.L.V. & Kennedy, W.D., 1991. Regional-residual gravity anomaly separation using the minimum-curvature technique, *Geophysics,* **56**(2), 279–283.

Mikhailov, V., Pajot, G., Diament, M. & Price, A., 2007. Tensor deconvolution: a method to locate equivalent sources from full tensor gravity data, *Geophysics,* **72**(5), I61–I69.

Nagy, D., 1966. The gravitational attraction of a right rectangular prism, *Geophysics,* **31**(2), 362–371.

Neumann, G.A., Zuber, M.T., Smith, D.E. & Lemoine, F.G., 1996. The lunar crust: global structure and signature of major basins, *J. geophys. Res.,* **101**(E7), 16 841–16 863

Pasckert, J.H., Hiesinger, H. & van der Bogert, C.H., 2018. Lunar farside volcanism in and around the South Pole–Aitken basin, *Icarus,* **299,** 538–562.

Pawlowski, R.S., 1994. Greens' equivalent layer concept in gravity bandpass filter design, *Geophysics,* **59**(1), 69–76.

Pawlowski, R.S. & Hansen, R.O., 1990. Gravity anomaly separation by Wiener filtering, *Geophysics,* **55**(5), 539–548.

Pieters, C., Head, J., Gaddis, L., Jolliff, B. & Duke, M., 2001. Rock types of South Pole-Aitken basin and extent of basaltic volcanism, *Journal of Geophysical Research: Planets,* **106**(E11), 28 001–28 022.

Pilkington, M. & Cowan, D.R., 2006. Model-based separation filtering of magnetic data, *Geophysics,* **71**(2), L17–L23.

Smith, D.E. *et al.*, 2010. Initial observations from the lunar orbiter laser altimeter (LOLA), *Geophys. Res. Lett.,* **37**(18), L18204, doi:10.1029/2010GL043751.

Soderblom, J.M. *et al.*, 2015. The fractured Moon: production and saturation of porosity in the lunar highlands from impact cratering, *Geophys. Res. Lett.,* **42**(17), 6939–6944.

Sood, R., Chappaz, L., Melosh, H.J., Howell, K.C., Milbury, C., Blair, D.M. & Zuber, M.T., 2017. Detection and characterization of buried lunar craters with GRAIL data, *Icarus,* **289,** 157–172.

Ucan, O.N., Seker, S., Albora, A.M. & Ozmen, A., 2000. Separation of magnetic fields in geophysical studies using a 2-D multi-resolution wavelet analysis approach, *J. Balkan Geophys. Soc.,* **3**(3), 53–58.

Von Frese, R.R., Hinze, W.J. & Braile, L.W., 1981. Spherical earth gravity and magnetic anomaly analysis by equivalent point source inversion, *Earth planet. Sci. Lett.,* **53**(1), 69–83.

Wieczorek, M.A. & Simons, F.J., 2005. Localized spectral analysis on the sphere, *Geophys. J. Int.,* **162**(3), 655–675.

Wieczorek, M.A. *et al.*, 2013. The crust of the moon as seen by GRAIL, *Science,* **339**(6120), 671–675.

Wu, W., Wang, Q., Tang, Y., Yu, G., Liu, J., Zhang, W. & Lu, L., 2017. Design of Chang'e-4 lunar farside soft-landing mission, *J. Deep Space Explor.,* **4**(2), 111–117.

Xia, J. & Sprowl, D.R., 1991. Correction of topographic distortion in gravity data, *Geophysics,* **56**(4), 537–541.

Xu, Y., Hao, T.Y., Li, Z.L., Duan, Q.L. & Zhang, L.L., 2009. Regional gravity anomaly separation using wavelet transform and spectrum analysis, *J. Geophys. Eng.,* **6**(3), 279–287.

Yingst, R., Chuang, F., Berman, D. & Mest, S., 2017. Geologic mapping of the Planck quadrangle of the Moon (LQ-29), in *Lunar and Planetary Science Conference,* **Vol. 48,** The Woodlands, TX.

Zeng, H.L., Xu, D.S. & Tan, H.D., 2007. A model study for estimating optimum upward continuation height for gravity separation with application to a Bouguer gravity anomaly over a mineral deposit, Jilin province, northeast China, *Geophysics,* **72**(4), I45–I50.

Zhang, L.L., Hao, T.Y. & Jiang, W.W., 2009. Separation of potential field data using 3-D principal component analysis and textural analysis, *Geophys. J. Int.,* **179**(3), 1397–1413.

Zhang, Y., Mooney, W.D. & Chen, C., 2018. Forward calculation of gravitational fields with variable resolution 3D density models using spherical triangular tessellation: theory and applications, *Geophys. J. Int.,* **215**(1), 363–374.

Zhang, Y., Mooney, W.D., Chen, C. & Du, J., 2019. Interface inversion of gravitational data using spherical triangular tessellation: an application for the estimation of the Moon's crustal thickness, *Geophys. J. Int.,* **217**(1), 703–713.

Zuber, M.T., Smith, D.E., Lemoine, F.G. & Neumann, G.A., 1994. The shape and internal structure of the moon from the Clementine mission, *Science,* **266**(5192), 1839–1843.